

Cite this: *RSC Adv.*, 2014, 4, 35493

Solution-processed reduced graphene oxide in light-emitting diodes and photovoltaic devices with the same pair of active materials

Sudip K. Saha,^a Saikat Bhaumik,^a Tanmoy Maji,^b Tarun K. Mandal^b and Amlan J. Pal^{*a}

We have introduced organic-dispersed reduced graphene oxides (rGO) in light-emitting diodes and photovoltaic devices. Both the devices were based on a conjugated polymer and inorganic nanoparticles. While we used a derivative of poly(*para*-phenylenevinylene) (MEH-PPV) as the organic semiconductor, zinc diffused copper indium disulphide (CIZS) quantum dots have been used as the inorganic counterpart that were based on nontoxic elements. We have shown that the device architecture in relation to rGO determines the functionality of a device based on the hybrid materials. A layer of rGO acted as a hole transport layer in MEH-PPV/CIZS heterojunction LEDs. On the other hand, the carbon allotrope added to MEH-PPV:CIZS bulk-heterojunction quenched photoluminescence of the components through a photoinduced electron-transfer process thereby dissociating photogenerated excitons yielding PV properties. The power conversion efficiency maximized at an optimum rGO concentration. The results show the role of reduced graphene oxides with the same pair of active materials in light-emitting diodes and photovoltaic devices.

Received 29th April 2014
Accepted 6th August 2014

DOI: 10.1039/c4ra03913k

www.rsc.org/advances

1. Introduction

In recent years, monomolecular sheets of graphite oxide that have been termed graphene oxides (GO) as an analogy to graphene, are being used in a range of devices due to their extraordinary electronic properties. In this direction, graphene oxides have been considered either as an electrode material^{1–6} or in the active layer in conjunction with quantum dots or organic semiconductors.^{7–16} The range of devices include, organic light-emitting diodes (LEDs) and quantum dot LEDs,^{2,3,7,8} dye-sensitized solar cells (DSSCs) and quantum-dot sensitized solar cells (QDSSCs),^{4,9–12} photodetectors,⁵ gas sensing,¹⁷ memory,¹⁸ charge storage,¹⁹ and organic photovoltaic devices (PVs) and quantum dot solar cells (QDSCs).^{1,6,13–16,20} In solar cells based on graphene oxides, they are being used as an electrode or an electron-acceptor, or light-absorber. The device configuration has been either Schottky junction⁶ or bulk-heterojunction with suitable organic or QDs so that an appropriate energy level diagram is formed.^{1,13–15,20} Integration of LEDs and PVs has also been carried out in a related direction.²¹

When we compare the device architecture of GO-based LEDs and PV devices, it appears that in LEDs, an interfacial layer of GO has been used to form a heterojunction device.⁸ In PV devices, on the other hand, a bulk-heterojunction was formed

between GOs and a suitable conjugated organics or QDs for improved absorption of solar illumination followed by harvesting of charge carriers. In most of the devices, cadmium based colloidal quantum dots were used for the ease of the growth process.^{9,13} The active material in the two devices was however not the same. In this work, we aimed to use a single pair of active materials to study the role of GO in both LEDs and PVs. We chose a derivative poly(*para*-phenylenevinylene) (PPV) as the organic semiconductor. As the inorganic counterpart, we used nontoxic elements to form zinc diffused copper indium disulfide (CIZS) quantum dots that have earlier been used in LEDs.^{22,23} We aimed to study on the location of GO in a sandwiched structure that would determine the functionality of the device, that is, the sandwiched structure acting as LEDs or PV devices.

2. Experimental

Materials

Copper(i) acetate, Cu(OAc) (97%), indium(iii) acetate, In(OAc)₃ (99.99%), zinc(ii) acetate, Zn(OAc)₂ (99.99%), sulphur powder (99.9%), dodecanethiol (DDT, >98%), oleylamine, and 1-octadecene (ODE), required to form CIZS nanocrystals, were purchased from Sigma-Aldrich. Graphite powder was purchased from Alfa Aesar. Sodium nitrate, sulfuric acid (H₂SO₄), potassium permanganate (KMnO₄), and H₂O₂ were purchased from Merck. Hexadecylamine (HDA) was purchased from Sigma-Aldrich. Poly [2-methoxy-5-(2-ethylhexyloxy)-1,4-phenylenevinylene] (MEH-PPV) were also purchased from Sigma-Aldrich. The polymer

^aDepartment of Solid State Physics, Indian Association for the Cultivation of Science, Jadavpur, Kolkata 700032, India. E-mail: sspajp@iacs.res.in

^bPolymer Science Unit, Indian Association for the Cultivation of Science, Jadavpur, Kolkata 700032, India

had an average molecular weight of 40 000–70 000. All the chemicals were used without further purification. The devices were formed on indium tin oxide (ITO) coated glass substrates that had a surface resistance of $15 \Omega \square^{-1}$.

Growth of CIZS nanocrystals

Colloidal CIZS nanocrystals were grown following a reported route.^{24,25} In brief, sulphur stock solution was formed by dissolving 0.3 mmol of sulphur (9 mg) in 0.5 mL of oleylamine and 2 mL of ODE under an inert environment. The mixture was heated to 100–120 °C that turned the mixture to a clear solution. To obtain a stock solution of indium, 1 mmol (292 mg) of $\text{In}(\text{OAc})_3$ was dissolved in 3.2 mL of oleic acid and 6.8 mL of ODE. The mixture, after degassing by purging ultra-high pure nitrogen (99.99%) for 15 min, was warmed mildly that turned the solution light yellow in color. Similarly, to obtain a stock solution of zinc, 0.1 mmol (220 mg) of $\text{Zn}(\text{OAc})_2$ was dissolved in 2 mL oleylamine and 8 mL ODE followed by degassing and a gentle heating.

In a typical reaction process to grow CIZS nanocrystals, 0.1 mmol (18 mg) $\text{Cu}(\text{OAc})_2$ was added to 2 mL of DDT and 5 mL of ODE. The reaction mixture, placed in a separate three-neck flask, was degassed in a similar fashion. 1 mL of indium solution was injected onto the mixture followed by an increase of the temperature of the reaction vial to 160 °C. Once the solution turned clear, 2.5 mL of sulfur stock solution was injected into the flask. The reaction was allowed to continue for 5 min with the color of the reactant turning dark-red indicating formation of CuInS_2 nanocrystals. At this stage, 2 mL of zinc stock solution was injected into the reaction mixture. The temperature of the reaction vial was increased to 210 °C to allow diffusion to zinc to the nanocrystals. The process of zinc diffusion or alloying was continued for 30 min to complete formation of zinc diffused copper indium disulfide (CIZS) nanocrystals. The flask was then cooled down to room temperature followed by purification using chloroform as solvents and ethanol and acetone as non-solvents. The nanocrystals were dispersed in chloroform for further analysis and use in devices.

Preparation of graphene oxides

Colloidal solution of graphene oxides was formed by Hummer's method.²⁶ A solid mixture of 100 mg of graphite powder and 50 mg of sodium nitrate was stirred for a day in 2.5 mL of concentrated sulfuric acid at room temperature. The temperature was then reduced to 0 °C; 300 mg of potassium permanganate was added under a vigorous stirring condition. After 20 min or so, the temperature of the solution was slowly raised to 35 ± 5 °C; while maintaining the temperature for 30 min, a brownish grey paste formed. At this stage, 5 mL of water was slowly added to the paste with an increase in temperature to 98 °C. A violent effervescence has resulted with the solution turning brownish yellow. The temperature of the solution was maintained at 98 °C for 15 min followed by an addition of 14 mL of warm water and 500 μL 3% hydrogen peroxide in sequence that reduced the unreacted permanganate. Light brownish-yellow particles were centrifuged at 14 000 rpm for 30 min

followed by washing in warm water until neutralization. The precipitates were air-dried followed by drying in vacuum at 70 °C. The solid powder was then exfoliated in 50 mL deionized water under sonication for 15 min; graphene oxides (GO) were centrifuged at 4000 rpm for 20 min for further functionalization with hexadecylamine (HDA).

To functionalize GO following a reported route,^{27,28} 50 mL GO suspension was mixed with a solution of HDA (150 mg) in 15 mL ethanol in a round bottom flask. The mixture was then refluxed for 20 h at 90 °C under a vigorous stirring condition. After the reaction was complete, the mixture was centrifuged at 10 000 rpm for 10 min to separate out HDA functionalized GO. The residual part was redispersed in 50 mL of ethanol, sonicated for 5 min, and centrifuged. The sequence of the processes was repeated several times to remove physically absorbed HDA completely. Finally, HDA functionalized GO that amounted to reduced graphene oxides (rGO) were obtained by drying the residue in vacuum at 70 °C.

Characterization of the nanoparticles

The materials were characterized with UV-Visible optical absorption spectroscopy, PL emission, transmission electron microscopy (TEM), X-ray photoelectron spectroscopy (XPS), Fourier transform infrared spectroscopy (FTIR) and Raman spectroscopy. The measurements were carried out with UV-Vis 2550 Shimadzu spectrometer, Spex Fluoromax 4P emission spectrophotometer, JEOL JEM-2100F, Omicron (serial number 0571), Shimadzu FTIR-8400S spectrometer, and Horiba Jobin-Yvon Raman triple grating spectrometer system (model T64000), respectively. Pellets for FTIR spectroscopy were prepared by mixing the corresponding dried sample with KBr in a 1 : 100 (w/w) ratio.

Device fabrication

Devices were fabricated on ITO coated glass substrates in the form of strips. The substrates were cleaned following a standard protocol. The entire device fabrication process was carried out inside a glove box that was equipped with a weighing balance, a magnetic stirrer, a hot-plate fitted with a temperature-controller, and a spin-coating unit. At first, a 30 nm layer of poly(3,4-ethylenedioxythiophene):poly(styrenesulfonate), PEDOT:PSS (Baytron P 4083), was spun on ITO substrates at a speed of 5000 rpm. The PEDOT:PSS films were annealed at 150 °C for 15 min on a hot-plate. To form a layer of the active material, a thoroughly mixed solution of MEH-PPV and CIZS nanocrystals and rGO (1 mg mL^{-1}) in chloroform having a weight ratio of 1 : 8 (MEH-PPV:CIZS) and a concentration of 20 mg mL^{-1} was spun on the PEDOT:PSS layer at a speed of 1500 rpm for 60 s. rGO was added to the MEH-PPV : CIZS solution at a measured weight ratio. For LEDs, a bilayer structure was formed on the PEDOT:PSS layer. To do so, layers of reduced GO, MEH-PPV, and CIZS nanocrystals were spun in sequence followed by annealing of the film at 140 °C after each step. Thickness of the nanocrystal layer was about 70 nm. Finally, a 100 nm film of aluminum (Al) as strips orthogonal to ITO electrodes was thermally evaporated under vacuum

($\sim 10^{-6}$ Torr) to complete fabrication of sandwiched-devices. Overlap of ITO and Al strips defined the area of the devices (4 mm^2). After aluminum evaporation, the devices were further annealed at 140°C for 20 min under the inert environment of the glove box.

Device characterization

To characterize the devices, the sandwiched structures were placed in a shielded metal-chamber under vacuum. Current-voltage (I - V) characteristics of the devices were recorded with a dc voltage source and a current meter (Keithley 6517 Electrometer). Luminous output of the LEDs was measured with a Konica Minolta Luminance Meter Model LS-110. To characterize PV devices, a chamber fitted with a quartz window was used for incidence of solar illumination. The instruments were operated with a PC through a general-purpose interface bus (GPIB). For PV devices, I - V characteristics were recorded also after illuminating the device. A solar simulator (Newport-Stratford model 67005) was used for this purpose. A Jobin-Yvon H20 monochromator was used to record the spectrum of the activity of the devices. Impedance spectroscopy of the devices was recorded with a Solartron Impedance Analyzer 1260A in the 10 Hz to 1 MHz region (8 points per decade) with 50 mV rms as a test voltage. The impedance analyzer was also controlled by a PC via a GPIB.

3. Results and discussion

Characterization of rGO

Formation of rGO was established by recording Raman spectrum of the sheets in spun-cast thin-films. Fig. 1 representing the Raman spectrum shows appearance of two prominent peaks at 1348.9 and 1598 cm^{-1} that are the well-documented D-band and G-band of rGO, respectively. While the D-band is associated with structural defects such as amorphous carbon or the edges that can break the symmetry and the selection rule, the G-band corresponds to the first-order scattering of the E_{2g} mode observed from sp^2 carbon domains. It can hence be inferred that highly disordered and randomly arranged graphene flakes were formed.

Valence state information and elemental composition of the reduced graphene oxides were studied by XPS analysis. Full

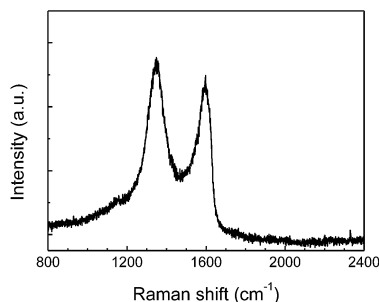


Fig. 1 Raman spectrum of rGO. Peaks at 1348.9 and 1598 cm^{-1} could be observed in the spectrum.

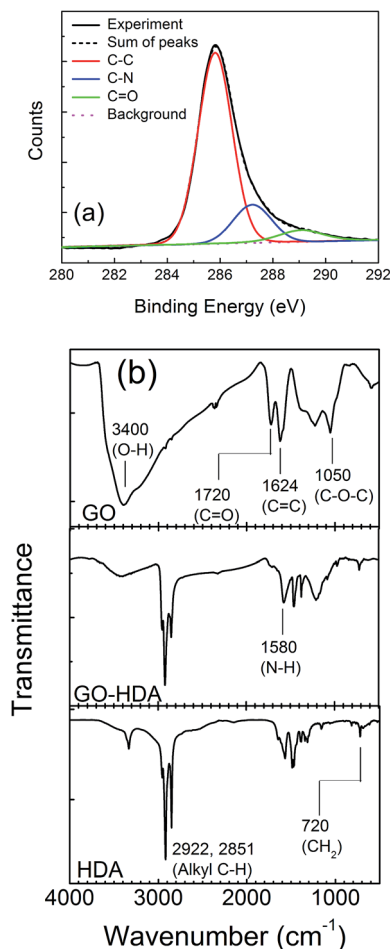


Fig. 2 (a) High-resolution XPS spectrum of rGO with deconvolution of the peaks. (b) FTIR spectra of GO, the HDA-functionalized GO, and the HDA ligand itself.

scan spectrum from rGO is shown in Fig. 2(a) that matches with a reported result.²⁹ Here, the binding energies obtained in the XPS analyses have been corrected by referencing the C1s peak to 285.8 eV . The peak in the region can be deconvoluted into three peaks with the major one being at 285.8 eV , which represents C-C bonds of carbon atoms in a conjugated honey-comb lattice. The other two peaks at 287.2 eV , and 289.2 eV represent the C-N and C=O bonding configurations, respectively. The C-N bonding in rGO confirms the complete reduction of the GO by HDA during the reaction process.

HDA functionalization of rGO was further established from FTIR studies as shown in Fig. 2(b). In this figure, we show spectrum of the GO, the HDA-functionalized GO, and the HDA ligand itself. Before the amine functionalization, the GO yielded bands at 3400 (O-H stretching), 1720 (C=O), 1624 (C=C), 1225 (C-OH), and 1050 cm^{-1} (C-O-C). In the HDA-functionalized GO, the bands characteristics to the HDA could be observed in addition to some of the bands of GO. The bands at 2922 and 2851 cm^{-1} corresponded to the C-H stretching of the alkyl chain; the other band at 720 cm^{-1} corresponds to CH_2 rock of the hexadecyl chain on rGO. In the HDA-functionalized GO, there has been a reduction in the intensity of the bands for

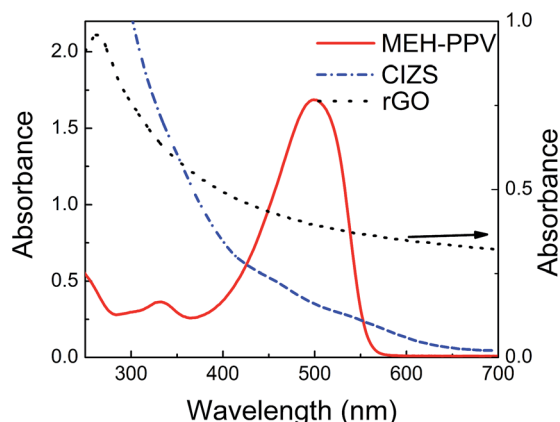


Fig. 3 Optical absorption spectrum of MEH-PPV and CIZS nanoparticles in (dispersed) solution along with that of reduced graphene oxides in dispersed solution (right scale).

C–O–C vibration ($900\text{--}1140\text{ cm}^{-1}$) and an emergence of a new band at 1580 cm^{-1} (–NH stretching vibration of –C–NH–C–bond) that overlaps with the stretching vibration of C=C bond as compared to the bare GO. This signifies a simultaneous functionalization and reduction of GO through a reaction between epoxide group of GO and the amine group of HDA. The FTIR results are in concurrence to the reported literature.²⁸

Optical absorption spectrum of reduced graphene oxides in dispersed solution is shown in Fig. 3. The figure includes spectra of the components of the devices, namely MEH-PPV and CIZS nanoparticles in dispersed solution. The spectra matched the reported results. We have also recorded PL emission spectrum of the components of the devices. Fig. 4(a) and (b) shows the PL spectra of MEH-PPV and CIZS in (dispersed) solution before and after the addition of rGO, respectively. Intensity of PL emission of the polymer and the nanoparticles decreased sharply upon the addition of rGO. Since the optical absorption of rGO and PL emission of the polymer and the nanocrystals did not overlap, energy transfer from MEH-PPV or CIZS to the rGO can be ruled out. The quenching of PL emission hence signifies electron-transfer from the polymer or nanocrystals to the graphene oxides. Such electron-transfer essentially means dissociation of excitons photogenerated in the active materials of the device that would be instrumental in the photovoltaic activity.

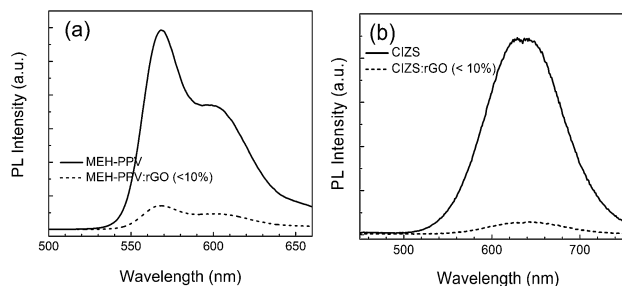


Fig. 4 Comparison of PL intensity between (a) MEH-PPV and MEH-PPV:rGO, (b) CIZS and CIZS-rGO both in chloroform solution.

TEM and HR-TEM

Fig. 5(a) and (b) show typical HR-TEM images of an rGO nanosheet and CIZS nanocrystals, respectively. In the image of rGO, ordered graphene lattices are clearly visible. The image of CIZS, on the other hand, shows uniform size distribution of the particles along with crystalline planes of the nanocrystals.

Light-emitting diodes

We have fabricated and characterized LEDs to study the role of rGO in the light-emitting devices. To do so, we formed bilayer structures with layers of MEH-PPV and CIZS sandwiched between ITO and Al electrodes as a standard device. To study the effect of rGO in the LEDs in transporting carriers (holes, in this case), we introduced a layer of the carbon allotrope in fabricating the devices. Current–voltage characteristics of the devices are shown in Fig. 6(a) for comparison. While the characteristics are nonlinear in nature, current at any voltage was higher in the device that had an additional layer of rGO. Since the operation of LEDs relies on injection of charge carriers, a facile hole injection improved light emission from the devices. We accordingly observed a lower turn-on voltage for the devices with a layer of rGO (Fig. 6(b)).

The spectra of external quantum efficiency (EQE), which is related to the internal quantum efficiency (IQE) as:

$$\text{EQE} = \text{IQE} \times R_e$$

is shown in the inset of Fig. 6(b). Here IQE is the number of photons produced in the device per number of electrons

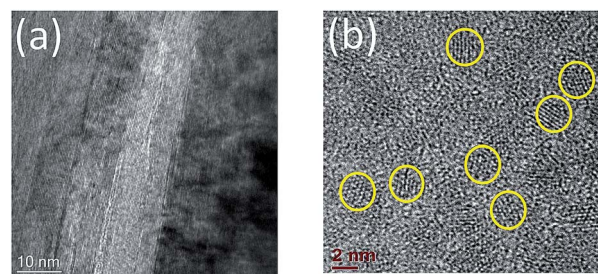


Fig. 5 HR-TEM images of (a) rGO and (b) CIZS nanoparticles.

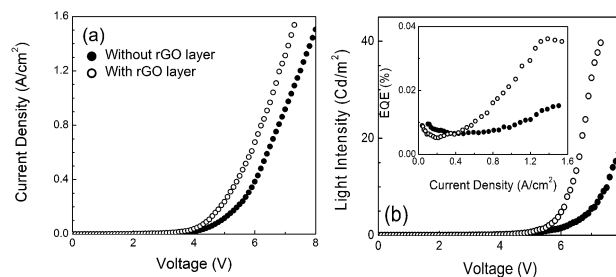


Fig. 6 (a) Current–voltage and (b) luminance–voltage characteristics of bilayer devices without and with a rGO layer, namely ITO/PEDOT:PSS/rGO/MEH-PPV/CIZS/Al and ITO/PEDOT:PSS/MEH-PPV/CIZS/Al. Inset of (b) shows EQE spectra of the devices.

injected into it and R_e is the extraction efficiency representing the number of photons transmitted out of the structure per number of photons generated. The EQE or the output of light emission was not as high as expected; it appears that the ligands present on the surface of nanoparticles might have hindered transport of electrons resulting in an imbalance in charge-transport and hence a lower luminance in the LEDs.

We have recorded EL spectra of the two devices (Fig. 7(a)). Intensity of the EL emission was much higher when the device contained rGO. Both the spectra resembled the PL spectrum of MEH-PPV/CIZS heterojunction implying that the excitons resided at the active materials before their radiative recombination. We recorded PL emission of thin-films of CIZS, MEH-PPH, and MEH-PPV/CIZS heterolayer for comparison (Fig. 7(b)). We observe that the higher energy part of the PL emission of MEH-PPV is absent in the spectrum of MEH-PPV/CIZS. In addition, a shoulder appeared in the spectrum of the heterojunction, the energy of which matches that of the peak of PL spectrum of CIZS nanocrystals. This implies that the PL emission MEH-PPV/CIZS heterojunction comprised emissions from both the components; higher energy part of the emission of MEH-PPV was however reabsorbed by the nanocrystals after a radiative recombination. The results hence infer that in the LEDs, upon facile hole transport through the rGO layer and electrons injection from the aluminum electrode, excitons formed in MEH-PPV and CIZS layers. Radiative recombination of the excitons occurred to yield EL emission. The higher energy component of EL emission from MEH-PPV was reabsorbed by the nanocrystals so that the EL had spectral characteristics of the MEH-PPV/CIZS heterojunction.

Photovoltaic devices

We then proceeded to fabricate and characterize PV devices with and without the rGO. The device on which we studied the effect of rGO was bulk-heterojunction device based on MEH-PPV and CIZS nanoparticles. In devices where rGO was added, the addition was made in the bulk-heterojunction so that excitons, photogenerated in both polymer and nanocrystals, may dissociate through an electron-transfer process to the rGO. We optimized the concentration of rGO in the active layer for improved PV performance. We first recorded I - V characteristics of the devices under a dark condition (Fig. 8(a)). The current at a

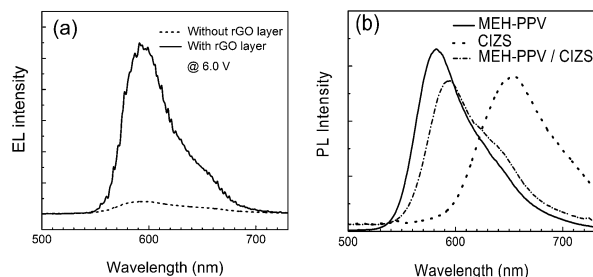


Fig. 7 (a) EL spectra of devices based on MEH-PPV/CIZS and rGO/ MEH-PPV/CIZS layers. (b) PL spectra of MEH-PPV, CIZS, and MEH-PPV/CIZS thin films.

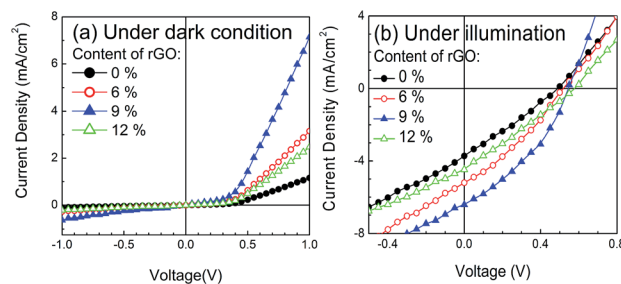


Fig. 8 Current-voltage characteristics of devices based on MEH-PPV:CIZS bulk-heterojunction with different content of rGO under (a) dark and (b) illumination condition.

voltage of the nonlinear I - V characteristics increased with an increase in the rGO content and went through a maximum. Upon illumination, all the devices acted as solar cells with the ITO and the Al as hole- and electron-collecting electrodes, respectively. While the open-circuit voltage (V_{OC}) remained unaltered with the content of rGO in the active layer, the short-circuit current (I_{SC}) depended strongly on the content. The I_{SC} was optimum at an intermediate value of rGO content in the bulk-heterojunction devices. The parameters of different solar cells have been collated in Table 1. The results hence show that the incorporation of rGO is beneficial to both LEDs and PVs, in which the same pair of active materials and electrodes were used. We can also infer that the device architecture in relation of the rGO has to be considered in deciding the functionality of the device.

To know the active materials in which photogeneration of excitons occurred in the PV devices, we recorded the spectra of external quantum efficiency (EQE) of the devices (Fig. 9). We then compared the EQE spectra with the optical absorption spectrum of the active layer of the devices. While the EQE spectra ranged up to 700 nm, the EQE at any wavelength was optimum at an intermediate value of rGO content at which the I_{SC} was also the highest. A comparison of the EQE spectra with the absorption spectra of the active layer reveals that the photogeneration of excitons in the both polymer and CIZS nanocrystals contributed to photovoltaic effect or short-circuit current in the external circuit.

We then moved to know the underlying mechanism involved in the improvement of PV performance upon the addition of rGO. To do so, we recorded impedance spectroscopy of the devices under dark and illumination conditions. No dc bias was

Table 1 Parameters of photovoltaic devices based on MEH-PPV:CIZS:rGO bulk-heterojunction with different content of rGO

Content of rGO in MEH-PPV:CIZS	I_{SC} (mA cm^{-2})	V_{OC} (V)	FF (%)	Power conversion efficiency (%)
0%	3.72	0.49	0.28	0.51
6%	5.20	0.51	0.32	0.67
9%	6.42	0.53	0.37	1.23
12%	4.47	0.57	0.27	0.84

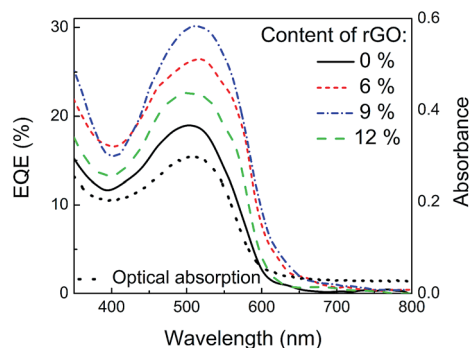


Fig. 9 EQE spectrum of devices based on MEH-PPV:CIZS bulk-heterojunction with different content of rGO. Optical absorption spectrum of a MEH-PPV:CIZS:rGO bulk-heterojunction thin-film has been added in the figure as a black dotted line for comparison.

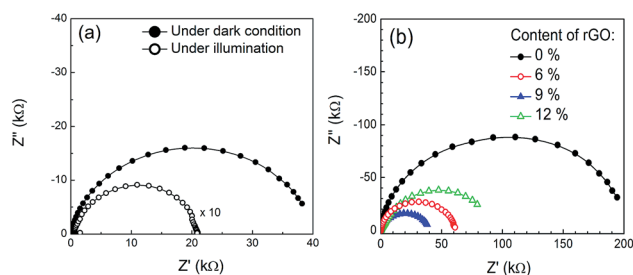


Fig. 10 (a) Plots of real and imaginary components of complex impedance of devices based on bulk-heterojunction of MEH-PPV:CIZS with 9% rGO under dark and illumination conditions. (b) The plots of devices with different content of rGO under a dark condition.

applied during the measurements. The plots between the real and the imaginary components of complex impedance (Nyquist plots) of the devices are presented in Fig. 10. All the plots are semicircular in nature suggesting that the devices could be modeled as a combination of a resistor and a capacitor in parallel. The diameter of the semicircles with the abscissa represents the bulk resistance of the device. The plots show that the bulk resistance decreased upon illumination (Fig. 10(a)). The sharp decrease in device resistance under illumination has occurred due to generation of free carriers upon exciton dissociation in the device. From the plots presented in Fig. 10(b), we observe that the diameter of the arc decreases and went through an optimum when rGOs were incorporated in the active layer of bulk-heterojunction device. Since the diameter of the semicircles with the abscissa represents bulk resistance of the device, the results hence are in concurrence with that obtained in I - V characteristics (Fig. 8(a)).

4. Conclusions

In conclusion, while introducing organic-dispersed rGO in LEDs and PV devices, we have shown that the device architecture in relation to the rGO has to be considered in deciding on the functionality of optoelectronic devices. Here, we have used the same pair of active materials, namely MEH-PPV and CIZS

nanoparticles to study the characteristics of the hybrid devices. For LEDs, we used a layered structure of the active materials along with a layer of rGO as a hole-transport layer that led to a decrease in turn-on voltage and increase in the EL output. In PV devices, the rGO, used in the bulk-heterojunction of the two materials, acted as an electron-acceptor to both the active materials. While tuning the content of rGO in the PV devices, the power conversion efficiency maximized at an optimum rGO concentration.

Acknowledgements

The authors acknowledge financial assistance from DeitY and SERIUS projects. The work of SB and TM were funded by CSIR – Junior Research Fellowship of Government of India.

References

- 1 J. B. Wu, H. A. Becerril, Z. N. Bao, Z. F. Liu, Y. S. Chen and P. Peumans, *Appl. Phys. Lett.*, 2008, **92**, 263302.
- 2 J. B. Wu, M. Agrawal, H. A. Becerril, Z. N. Bao, Z. F. Liu, Y. S. Chen and P. Peumans, *ACS Nano*, 2010, **4**, 43.
- 3 A. V. Klekachev, S. N. Kuznetsov, I. Asselberghs, M. Cantoro, J. H. Mun, B. J. Cho, A. L. Stesmans, M. M. Heyns and S. De Gendt, *Appl. Phys. Lett.*, 2013, **103**, 043124.
- 4 H. Choi, H. Kim, S. Hwang, W. Choi and M. Jeon, *Sol. Energy Mater. Sol. Cells*, 2011, **95**, 323.
- 5 C. C. Lin, D. Y. Wang, K. H. Tu, Y. T. Jiang, M. H. Hsieh, C. C. Chen and C. W. Chen, *Appl. Phys. Lett.*, 2011, **98**, 263509.
- 6 Y. Ye, Y. Dai, L. Dai, Z. J. Shi, N. Liu, F. Wang, L. Fu, R. M. Peng, X. N. Wen, Z. J. Chen, Z. F. Liu and G. G. Qin, *ACS Appl. Mater. Interfaces*, 2010, **2**, 3406.
- 7 D. I. Son, B. W. Kwon, D. H. Park, W. S. Seo, Y. Yi, B. Angadi, C. L. Lee and W. K. Choi, *Nat. Nanotechnol.*, 2012, **7**, 465.
- 8 D. Y. Wang, I. S. Wang, I. S. Huang, Y. C. Yeh, S. S. Li, K. H. Tu, C. C. Chen and C. W. Chen, *J. Phys. Chem. C*, 2012, **116**, 10181.
- 9 S. R. Sun, L. A. Gao, Y. Q. Liu and J. Sun, *Appl. Phys. Lett.*, 2011, **98**, 093112.
- 10 H. B. Yang, G. H. Guai, C. X. Guo, Q. L. Song, S. P. Jiang, Y. L. Wang, W. Zhang and C. M. Li, *J. Phys. Chem. C*, 2011, **115**, 12209.
- 11 H. H. Niu, S. W. Zhang, Q. Ma, S. X. Qin, L. Wan, J. Z. Xu and S. D. Miao, *RSC Adv.*, 2013, **3**, 17228.
- 12 K. Jayawardena, R. Rhodes, K. K. Gandhi, M. R. R. Prabhat, G. Dabera, M. J. Beliat, L. J. Rozanski, S. J. Henley and S. R. P. Silva, *J. Mater. Chem. A*, 2013, **1**, 9922.
- 13 C. X. Guo, H. B. Yang, Z. M. Sheng, Z. S. Lu, Q. L. Song and C. M. Li, *Angew. Chem., Int. Ed.*, 2010, **49**, 3014.
- 14 V. Gupta, N. Chaudhary, R. Srivastava, G. D. Sharma, R. Bhardwaj and S. Chand, *J. Am. Chem. Soc.*, 2011, **133**, 9960.
- 15 J. Wang, X. K. Xin and Z. Q. Lin, *Nanoscale*, 2011, **3**, 3040.
- 16 Q. D. Yang, T. W. Ng, M. F. Lo, N. B. Wong and C. S. Lee, *Org. Electron.*, 2012, **13**, 3220.
- 17 Q. M. Ji, I. Honma, S. M. Paek, M. Akada, J. P. Hill, A. Vinu and K. Ariga, *Angew. Chem., Int. Ed.*, 2010, **49**, 9737.

- 18 M. A. Mamo, A. O. Sustaita, N. J. Coville and I. A. Hummelgen, *Org. Electron.*, 2013, **14**, 175.
- 19 K. Kume, N. Kawasaki, H. Wang, T. Yamada, H. Yoshikawa and K. Awaga, *J. Mater. Chem. A*, 2014, **2**, 3801.
- 20 P. Wang, T. F. Jiang, C. Z. Zhu, Y. M. Zhai, D. J. Wang and S. J. Dong, *Nano Res.*, 2010, **3**, 794.
- 21 X. Z. Wang, H. L. Tam, K. S. Yong, Z. K. Chen and F. R. Zhu, *Org. Electron.*, 2011, **12**, 1429.
- 22 Z. Tan, Y. Zhang, C. Xie, H. Su, J. Liu, C. Zhang, N. Dellas, S. E. Mohny, Y. Wang, J. Wang and J. Xu, *Adv. Mater.*, 2011, **23**, 3553.
- 23 B. K. Chen, H. Z. Zhong, W. Q. Zhang, Z. A. Tan, Y. F. Li, C. R. Yu, T. Y. Zhai, Y. S. Bando, S. Y. Yang and B. S. Zou, *Adv. Funct. Mater.*, 2012, **22**, 2081.
- 24 J. Zhang, R. G. Xie and W. S. Yang, *Chem. Mater.*, 2011, **23**, 3357.
- 25 L. De Trizio, M. Prato, A. Genovese, A. Casu, M. Povia, R. Simonutti, M. J. P. Alcocer, C. D'Andrea, F. Tassone and L. Manna, *Chem. Mater.*, 2012, **24**, 2400.
- 26 W. S. Hummers and R. E. Offeman, *J. Am. Chem. Soc.*, 1958, **80**, 1339.
- 27 Z. Y. Lin, Y. Liu and C. P. Wong, *Langmuir*, 2010, **26**, 16110.
- 28 W. J. Li, X. Z. Tang, H. B. Zhang, Z. G. Jiang, Z. Z. Yu, X. S. Du and Y. W. Mai, *Carbon*, 2011, **49**, 4724.
- 29 D. R. Dreyer, S. Park, C. W. Bielawski and R. S. Ruoff, *Chem. Soc. Rev.*, 2010, **39**, 228.